RESEARCH ARTICLE OPEN ACCESS

Structure and Facet Characterization of Platinum Nanoparticles Loaded on Carbon Black Particles using HRTEM

Kun'ichi Miyazawa*,Shuichi Shimomura**, Masaru Yoshitake*,Yumi Tanaka*
**Department of Industrial Chemistry, Faculty of Engineering, Tokyo University of Science, Tokyo 162-0826, Japan*
*** National Institute for Materials Science (NIMS), Tsukuba 305-0044, Japan*
Corresponding Author: Kun'ichi Miyazawa

ABSTRACT
The atomic structure of platinum nanoparticles (Pt NPs) loaded on carbon black (CB) particles was investigated using high-resolution transmission electron microscopy (HRTEM). The Pt NPs were inhomogeneously strained and approximated as monoclinic structures. No correlation was observed between the monoclinic lattice parameters and the size of Pt NPs. About 80 % of the Pt NPs were compressively strained, and about 20 % of the Pt NPs were expansively strained. Side-view HRTEM analyses of Pt NPs were performed for specimens milled by a focused ion beam apparatus (FIB). The (111), (100), and (110) facets of the Pt NPs were observed to be adhered to CB particles. The frequency of Pt NP-CB adhesion interfaces decreased in the order of (111), (100), and (110) facets. This order was consistent with the (111), (100), and (110) planar packing fractions of Pt, the observed frequencies of (111), (100), and (110) facets of Pt NPs, and the (111), (100), and (110) surface energies of Pt. Further, variation of (111) interplanar spacing of Pt NPs on CB particles was measured as a function of azimuth angle of the (111) planes, and no correlation was observed between the variation of (111) interplanar spacing and the azimuth angle.
Keywords - Fuel cell, HRTEM, platinum nanoparticle, structure, TEC10E50E

Date Of Submission:02-11-2018 Date Of Acceptance:16-11-2018

I. INTRODUCTION

It has been reported that the lattice parameter of platinum nanoparticles (Pt NPs) decreases with decreasing nanoparticle size [1]. In order to examine this phenomenon, we deposited Pt NPs on graphite particles using a coaxial arc plasma gun in vacuum and analyzed the relationship between the particle size and face-centered cubic (FCC) lattice parameter of Pt NPs [2]. However, no correlation was observed between the two parameters through high-resolution transmission electron microscopy (HRTEM) observations. By fast Fourier transform (FFT) analyses of the cross-lattice fringes of Pt NPs, it was found that Pt NPs were inhomogeneously strained and that this anisotropic straining caused variation in the lattice parameters of Pt NPs. Hence, the lattices of Pt NPs deposited on graphite particles were approximated by monoclinic lattices and the HRTEM images of Pt NPs were analyzed. As a result, the mean value of the cube root of the monoclinic unit cell volume ($V^{1/3}$) of Pt NPs was found to be smaller than the FCC lattice parameter of bulk Pt, and it was found that approximately two-thirds of the Pt NPs were compressively strained and that the other Pt NPs were expansively strained. Further, the value of $V^{1/3}$ ranged from a compression of 5.9% to an expansion of 2.8% as compared with the lattice parameter of bulk Pt. The anisotropic straining of Pt NPs was also observed in the Pt NPs that were deposited on C_{60} fullerene nanowhiskers using the coaxial arc plasma gun [3].

It has been reported that the catalytic activity of Pt NPs is influenced by the lattice straining [4, 5] and that the Pt (110) facets with large tensile strains are favorable for the optimization of Pt-O bond strength that affects the ORR activity [6]. It is of interest to know how the crystal structure of Pt NPs is strained even in practical catalysts. In addition, since it has been reported that the oxygen reduction reaction (ORR) activity of Pt single crystal facets reduces in the order of Pt (111) ≈ Pt (110) > Pt (100) [7] and that Pt {110} surfaces are more active than Pt {111} and {100} surfaces for the ORR in perchloric acid [6, 8], it is of interest to know what facets more frequently appear in practical Pt catalysts. To our knowledge, however, no report on the statistical data of Pt NP facets in practical catalysts have been published yet. Hence, the current study is focused on the structural characterization of Pt NPs supported on carbon black (CB) particles in a commercially available catalyst. To conduct the above study, Pt NPs from TEC10E50E powder milled by a focused ion beam apparatus (FIB) were

investigated in addition to those of as-received TEC10E50E powder. Detailed structural analyses of Pt NPs on CB particles on the atomic scale are presented in this paper.

II. EXPERIMENTAL PROCEDURES

A portion of as-received TEC10E50E powder (Tanaka Kikinzoku Kogyo K.K., Tokyo, Japan) was ultrasonically dispersed in ethanol and pipetted onto TEM carbon microgrids. The TEC10E50E powder samples on TEM microgrids were observed using a high-resolution transmission electron microscope (JEOL JEM2800, 200 kV).

On the other hand, a portion of the as-received TEC10E50E powder was ultrasonically dispersed into a solution of 0.24 mL water and 0.76 mL isopropyl alcohol, and the ultrasonicated TEC10E50E powder was deposited on the flat surface of a glassy carbon electrode (4 mm in diameter and 4 mm in height). A thin layer (~500 nm thick) of tungsten was coated on the deposited TEC10E50E powder using a focused ion beam milling apparatus (FIB-SEM, Hitachi NB5000, Japan), and then the W-coated TEC10E50E powder was milled to a thickness of less than 100 nm with a Ga ion beam (40 keV) to facilitate the observation of Pt NP-CB particle adhesion at the interface.

The measurement of particle size and monoclinic lattice parameters of Pt NPs was conducted using the same method described in ref. [2]. The magnification of the HRTEM images was calibrated using high-purity silicon (Si) crystals (Optostar Ltd, Tsukuba, Japan). Every HRTEM image was taken at a nominal magnification of 1,000,000.

HRTEM image simulation was conducted using self-developed software based on the eigenvalue method [9].

III. RESULTS AND DISCUSSION

Figure 1 (a) displays an example of HRTEM image of a Si crystal that was observed along the [110] zone axis. Using the FFT spots as shown in Fig. 1 (b), the actual magnification of the TEM was measured. 55 FFT spots from different lattice images of Si crystals were analyzed, where (111), (200), (220) and (311) FFT spots were used for the magnification measurement. Figure 2 displays the distribution of measured magnifications which ranged from 9.51×10^5 to 1.02×10^6 and the mean magnification was $9.80\times10^5 \pm 0.15\times10^5$ (mean ± sd). The histogram could be fitted by the normal distribution curve, which means that 95.5% of the observations involved magnification fluctuations of about 3% around the mean magnification of 9.80×10^5 in this study.

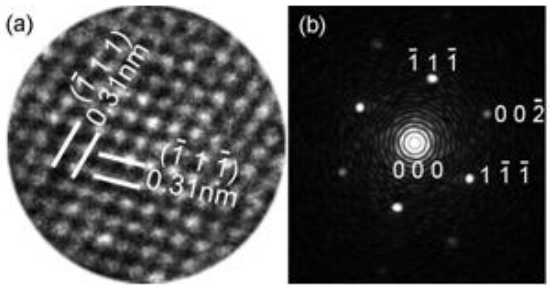

Fig. 1. (a) HRTEM image of Si crystal taken at a nominal magnification of 1,000,000. (b) FFT image for (a).

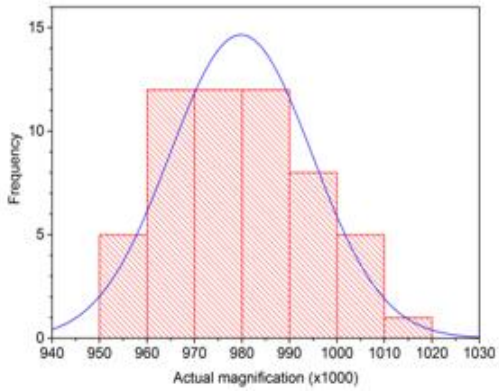

Fig. 2. Distribution of the actual magnifications measured using FFT images of the Si lattice images taken at a nominal magnification of 1,000,000.

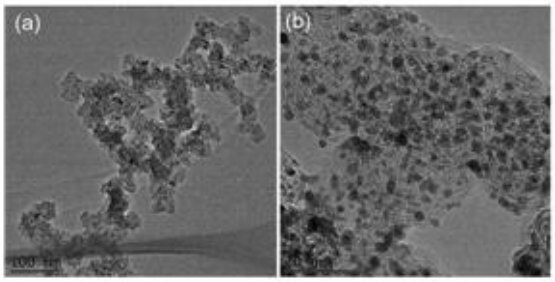

Fig. 3. (a) TEM image of TEC10E50E powder, (b) magnified TEM image of TEC10E50E powder.

Figure 3 (a) displays an example TEM image of the as-received TEC10E50E powder. Figure 3 (b) is a magnified image of TEC10E50E showing the CB particles with spherically stacked graphene layers and Pt NPs.

Figure 4 (a) displays a part of the as-received TEC10E50E powder showing the CB particles with Pt NPs. A Pt NP with cross-lattice fringes indicated by arrow is displayed in the magnified image of Fig. 4 (b). The lattice planes indicated by $(1\bar{1}\bar{1})$ and $(1\bar{1}1)$ are observed to be curved, showing that the Pt NP is inhomogeneously strained. Figure 4 (c) displays a fast Fourier transform (FFT) pattern of the strained Pt NP (Fig. 4

(b)) showing the incident electron beam direction parallel to the [110] zone axis, where measured interplanar angles are indicated. In FCC crystals, the interplanar angle between the (002) and $(1\bar{1}1)$ planes is 54.7° and that between the $(1\bar{1}1)$ and $(1\bar{1}\bar{1})$ planes is 70.5°. However, the measured angles shown in Fig. 4 (c) are 56.2° between the (002) and $(1\bar{1}1)$ planes and 70.2° between the $(1\bar{1}1)$ and $(1\bar{1}\bar{1})$ planes, slightly deviating from the theoretical angles, indicating the anisotropic straining of the Pt NP.

HRTEM images with cross-lattice fringes taken along the [110] zone axes were obtained for 134 Pt NPs of the as-received TEC10E50E. Using the FFT images as shown in Fig. 4 (c), lattice plane spacings of $d(1\bar{1}\bar{1})$ and $d(1\bar{1}1)$ were calculated. A parameter S indicating the anisotropic strain in the (110) lattice plane was defined by the ratio between $d(1\bar{1}\bar{1})$ and $d(1\bar{1}1)$, and the values of S were calculated using the 134 cross-lattice images of the Pt NPs viewed along the [110] zone axis.

Figure 5 shows the distribution of S values, where $S = d(1\bar{1}\bar{1})/d(1\bar{1}1)$ or $S = d(1\bar{1}1)d(1\bar{1}\bar{1})$ so that $S \geq 1$. The value of S ranged from 1.00 to 1.16, and the mean value of S was 1.03 ± 0.03. On the other hand, using 11 cross-lattice images of different Si crystals that were viewed along the [110] zone axis as shown in Fig. 1, the S value was also measured, and the S value ranged from 1.00 to 1.02 with the mean value of 1.01 ± 0.01. This result shows that the anisotropic stain is negligibly small in the Si crystals as compared with the Pt NPs. Hence, it is no doubt that the Pt NPs were anisotropically strained from the correct FCC structure.

Figure 6 shows the size distribution of the 134 Pt NPs whose average diameter was measured to be 3.4 ± 0.9 nm, which well coincides with the mean diameter of 3.3 nm of the Pt NPs in TEC10E50E powder that was measured by XRD [10].

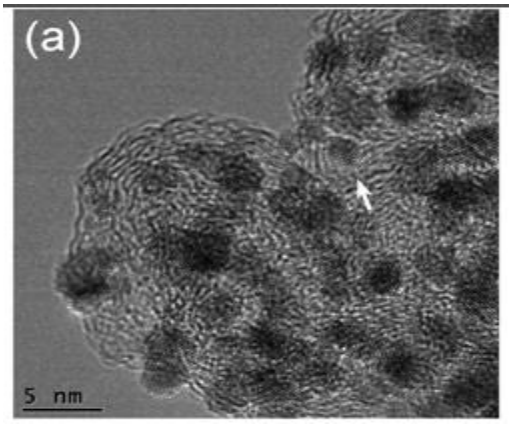

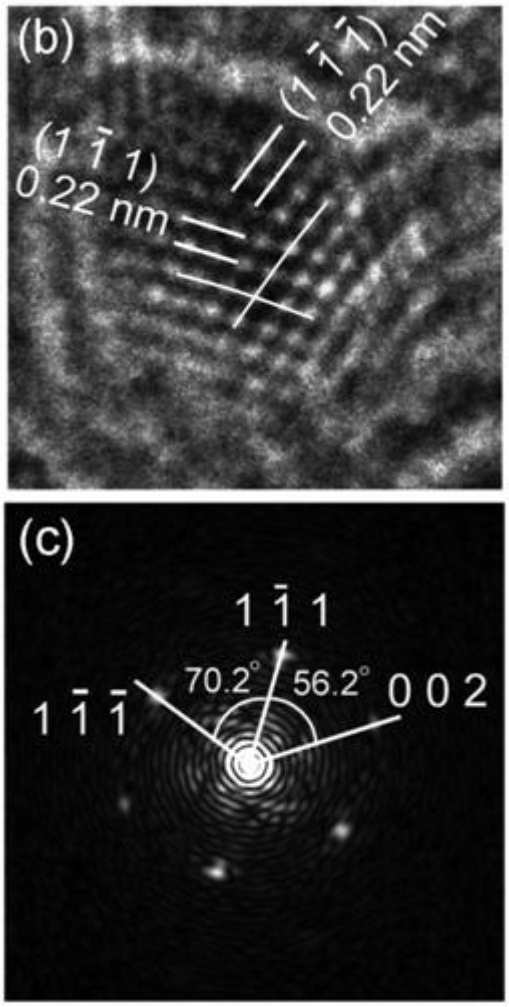

Fig. 4. (a) HRTEM image of a part of the as-received TEC10E50E powder, (b) magnified image of the arrowed Pt NP of (a), and (c) FFT pattern for the Pt NP of (b).

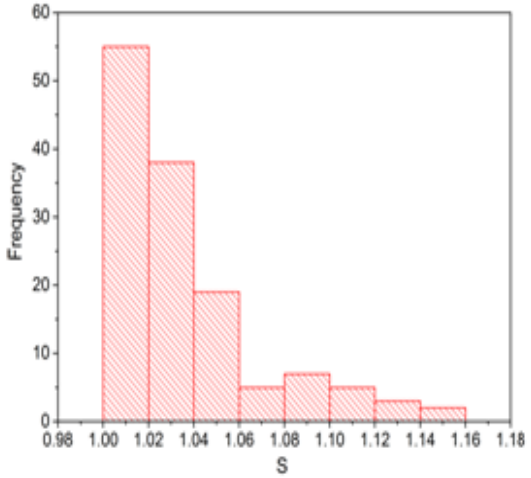

Fig. 5. Distribution of the anisotropic strain S in the (110) lattice plane of the Pt NPs.

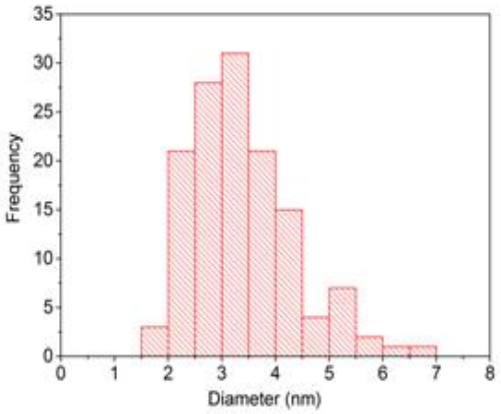

Fig. 6. Diameter distribution of the Pt NPs from the as-received TEC10E50E powder used for monoclinic lattice parameter measurements.

As described in our previous paper [2], the structure of Pt NPs was approximated as a monoclinic lattice and the lattice parameters (a (nm), b (nm), c (nm), β (°)) were obtained using the least squares method, i.e., the lattice plane spacings $d(1\bar{1}1)$, $d(1\bar{1}\bar{1})$ and d(002) were calculated so that F(a, b, c, β) (1) becomes minimum by varying a, b, c and β, using Mathematica (Wolfram), where d_0(hkl) means the (hkl) interplanar spacing measured from the observed HRTEM image.

$$F(a, b, c, \beta) \equiv (d_0(1\bar{1}1) - d(1\bar{1}1))^2 + (d_0(1\bar{1}\bar{1}) - d(1\bar{1}\bar{1}))^2 + (d_0(002)-d(002))^2 . \quad (1)$$

Figure 7 shows the results of fitting the monoclinic lattice parameters which are plotted as a function of particle diameter (D). The mean lattice parameters are a=0.373 ± 0.016 nm, b=0.377 ± 0.015 nm, c=0.406 ± 0.035 nm and β=93.7 ± 3.5°.

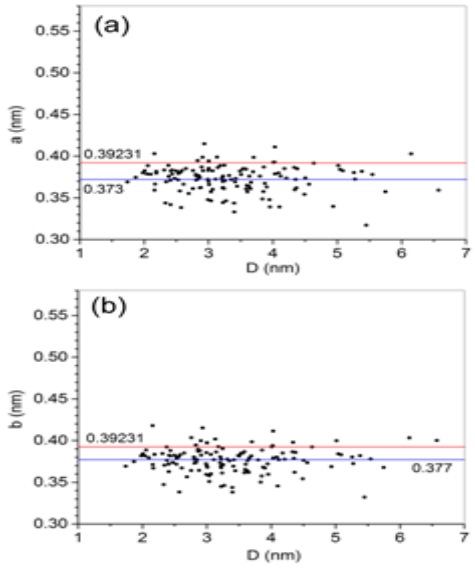

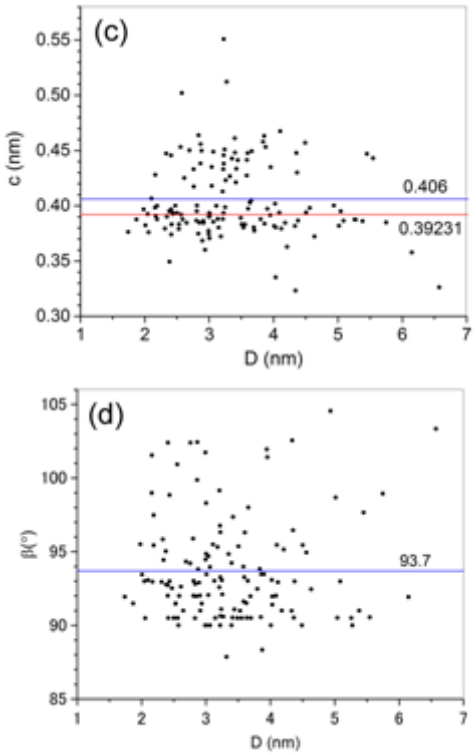

Fig. 7. Monoclinic lattice parameters a (nm), b (nm), c (nm), and β (°) of the Pt NPs from the as-received TEC10E50E powder plotted as a function of diameter D (nm).

No correlation is observed between the lattice parameters and the particle diameters. The wide scatter in the measured lattice parameters implies that the lattices are randomly strained irrespective of particle diameter.

The cube root of the monoclinic unit cell volume ($V^{1/3}$) for the Pt NPs is shown in Fig. 8 as a function of diameter. The mean value of $V^{1/3}$ is 0.384 ± 0.009 nm, which is approximately 2.1% smaller than the lattice parameter a_0 = 0.39231 nm of bulk Pt (JCPDS 00–004-0802). This result is consistent with the reported result that Pt NPs showed the lattice parameters less than a_0 [1]. The value of $V^{1/3}$ ranged from 0.356 nm to 0.405 nm in Fig. 8. The magnification of TEM may fluctuate in various ways according to the observation condition that changes depending on the focusing, sample position and stability of lens system. The calibrated magnification of TEM might have involved a fluctuation of ~3 % around 1.00×10^6. However, the scattering of $V^{1/3}$ of Fig. 8 is too wide as compared to the magnification fluctuation. Hence, it is clear that the wide distribution of $V^{1/3}$ was caused by the inhomogeneous straining of the Pt NPs.

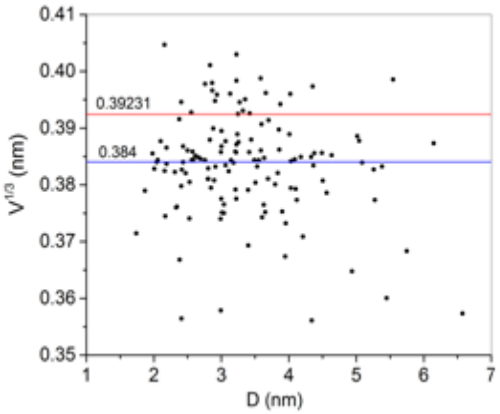

Fig. 8. Cube root of unit cell volume $V^{1/3}$ (nm) of the Pt NPs from the as-received TEC10E50E powder plotted as a function of diameter D.

The lattice strain of the Pt NPs, defined as $100(V^{1/3}-a_0)/a_0$ (%), was calculated and found to range from a compression of 9.2% to an expansion of 3.2%. Figure 9 shows the lattice strain distribution of Pt NPs, where it is shown that 83% of the Pt NPs are compressed and 17% of the Pt NPs are expanded.

Table 1 summarizes the measurement results. It is expected that expanded Pt unit cells are favorable for increasing the surface reactivity of Pt NPs with CO molecules [5, 11], and it has been reported that compressed Pt unit cells are favorable for enhancing the ORR activity of Pt NPs [4, 12]. In Table 1, about 80% of the Pt NPs are compressed and about 20% of the Pt NPs are expanded. For one Pt NP, this result implies that about 80% of the surface area of the Pt NP exhibits enhanced ORR activity and that about 20% of the surface area of the Pt NP is favorable for CO oxidation. It is considered that inhomogeneous strain can form both expanded facets and compressed facets in the same Pt NP. Hence, determining how to tailor the lattice strain of individual Pt NPs is of great importance for developing excellent Pt catalysts.

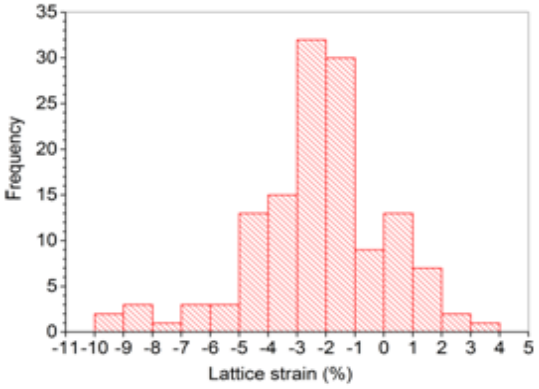

Fig. 9. Lattice strain distribution of the Pt NPs from the as-received TEC10E50E powder.

On the other hand, it has been reported that the ORR activity of Pt NPs can be enhanced by inducing a -2 to -3 % surface strain on their (111) surfaces [13]. In Table 1, mean compressive lattice strains similar to the above strains are shown for the Pt NPs of TEC10E50E. Moreover, the ORR activity has been known to change depending on the low-index Pt facets [14]. Hence, in studying the catalytic activity of Pt NPs, the surface characterization of Pt NPs is imperative in addition to the characterization of their crystal structure.

To know what facets of Pt NPs appear in TEC10E50E, side-view observations of Pt NPs were conducted. Figure 10 (a) shows a TEM image of FIB-processed CB particles where a layer of W was deposited for protection from the Ga ion beam. Figure 10 (b) shows an enlarged image of the FIB-processed CB particles whose surface has layers of loaded Pt NPs. A side view example of Pt NP adhered to the surface of a CB particle is shown Fig. 11 (a).

Table 1 Parameters measured for the Pt NPs of as-received TEC10E50E powder.

Diameter (nm)	a (nm)	b (nm)	c (nm)	β (°)	$V^{1/3}$ (nm)	Lattice strain (%)	Compressive lattice strain (%)	Expansive lattice strain (%)	Compressed Pt NPs (%)	Expanded Pt NPs (%)
3.4 ±0.9	0.373 ± 0.016	0.377 ± 0.015	0.406 ± 0.035	93.7 ± 3.5	0.384 ± 0.009	-2.2 ± 2.3	-2.9 ±1.9	1.1 ± 0.8	83	17

The body of the CB particle shown was milled by a FIB. The magnified image in Fig. 11 (b) shows the $(1\bar{1}\bar{1})$, (001), and $(1\bar{1}1)$ facets of the Pt NP. Although most of the adhesion facet appears disordered, a (001) facet of the Pt NP is shown to adhere to the CB particle. A simulated image was inserted to roughly estimate the thickness of the Pt NP, assuming a thickness of 4 nm and a defocus value of 10 nm over focusing (C_s = 0.7 mm).

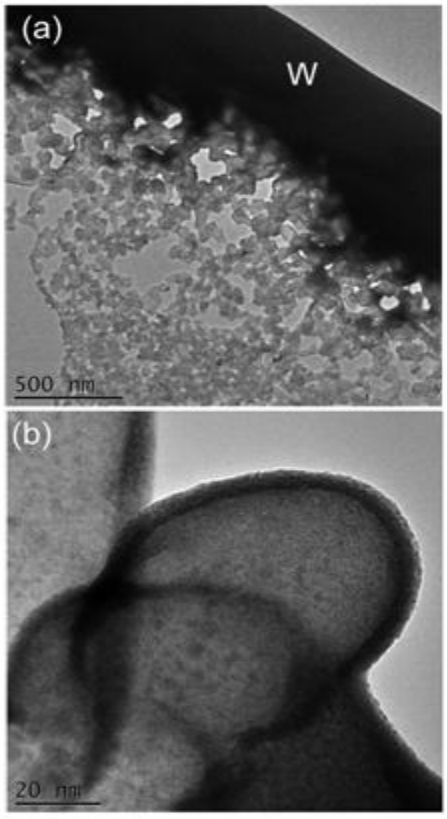

Fig. 10. (a) TEM image of CB particles prepared by milling TEC10E50E powder using a FIB. (b) Magnified TEM image of the CB particles milled by FIB.

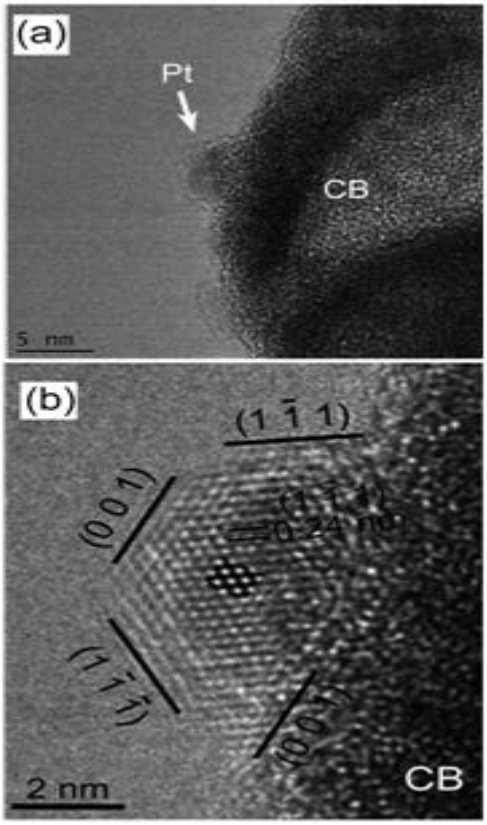

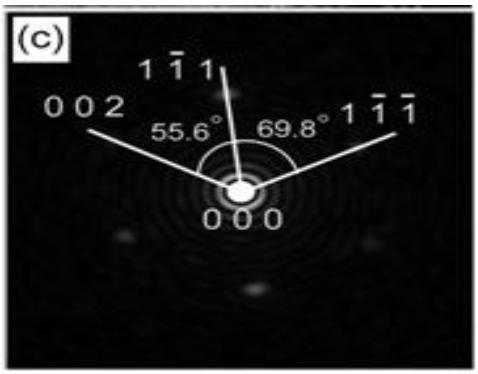

Fig. 11. (a) HRTEM image of a Pt NP adhered to the surface of CB particle in the FIB-processed TEC10E50E powder. (b) Magnified image of (a) with an inserted simulated image. (c) FFT image of the Pt NP shown in (b).

The monoclinic lattice parameters of the Pt NP were determined from the FFT image shown in Fig. 11 (c) using the least squares method, where values of a = 0.407 nm, b = 0.408 nm, c = 0.423 nm, and β = 92.7° were obtained. The cube root of the unit cell volume was calculated to be 0.413 nm, showing an expansive strain of 5.2 %.

Figure 12 shows other examples of Pt NPs whose facets are adhered to CB particle surfaces. Figure 12 (a) shows a Pt NP whose $(1\bar{1}\bar{1})$, $(1\bar{1}1)$, and (001) facets are adhered to the CB matrix. The inside $(1\bar{1}\bar{1})$ lattice planes are heavily distorted and show wavy structures. The Pt NP is surrounded by other $(1\bar{1}1)$, $(1\bar{1}0)$, and $(1\bar{1}\bar{1})$ surface facets. Figure 12 (b) shows a Pt NP whose $(1\bar{1}\bar{1})$, $(1\bar{1}1)$, and (001) facets are adhered to the CB matrix, and the Pt NP is also surrounded by other $(1\bar{1}1)$, (001), and $(1\bar{1}\bar{1})$ surface facets. Figure 12 (c) shows a Pt NP whose $(1\bar{1}0)$ facet is adhered to the CB matrix, and the Pt NP is also surrounded by (001), $(1\bar{1}\bar{1})$, and $(1\bar{1}1)$ surface facets. The curved facet indicated by the arrow is parallel to the $(1\bar{1}1)$ surface and expanding outward. These images show that the Pt NPs on CB particles are variously strained and locally deformed. These various inhomogeneous distortions of Pt NPs give rise to the scattered lattice parameter data.

As shown in the above examples, the {111}, {100} and {110} facets of Pt NPs were observed to be adhered to CB particles of TEC10E50E. Next, to know what facets are likely to adhere to CB particles and what facets of Pt NPs are likely to appear, 128 Pt NPs adhering to CB particles of FIB-processed TEC10E50E powder were analyzed and the frequency of each facet is plotted as a function of the planar packing fraction of Pt crystals in Fig. 13, where 462 facets of Pt NPs and 167 Pt NP-CB adhesion interfaces were analyzed.

The ratio of planar packing fractions of Pt crystals is 1.633:1.414:1 in the order of (111), (100) and (110) lattice planes. Figure 13 (a) shows the observed frequency of Pt NP facets plotted as a function of planar packing fraction, where a good linear correlation is observed between the two parameters. Figure 13 (b) shows the observed frequency of Pt NP-CB adhesion facet plotted as a function of planar packing fraction, which also shows a strong correlation between these two parameters. The order of observed frequency of facets is consistent with the surface energy, σ, of Pt crystals which decreases in the order of σ(110), σ(100), and σ(111) [15]. However, this result does not necessarily imply that the (111) facets of Pt NPs have a higher affinity for the CB surfaces, since the frequency of Pt NP-CB adhesion facets is strongly proportional to the frequency of Pt NP facets in Fig. 13 (c), which implies that the observed frequency order might have been caused by a probabilistic factor.

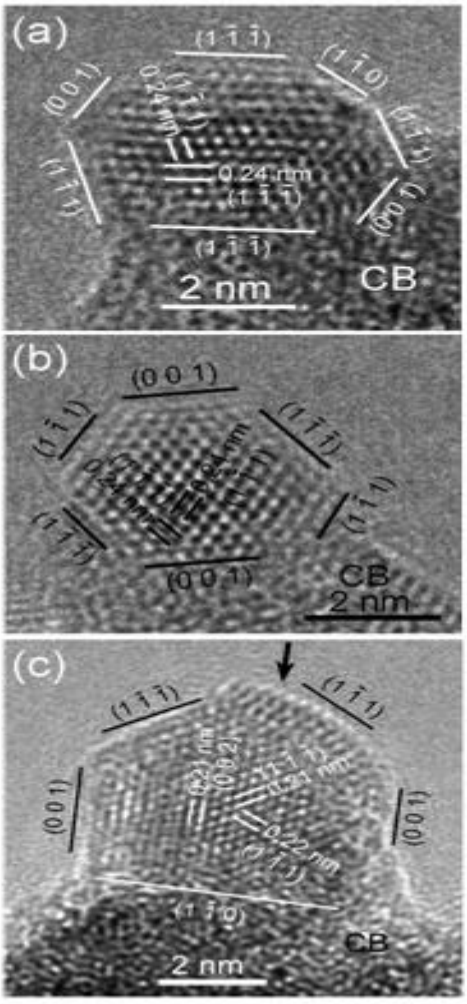

Fig. 12. HRTEM images of the FIB-processed TEC10E50E powder. (a) Pt NP adhered to CB matrix via $(1\bar{1}\bar{1})$ and (001) facets. (b) Pt NP adhered to CB matrix via $(1\bar{1}\bar{1})$, (001), and $(1\bar{1}1)$ facets. (c) Pt NP adhered to CB matrix via $(1\bar{1}0)$ facet.

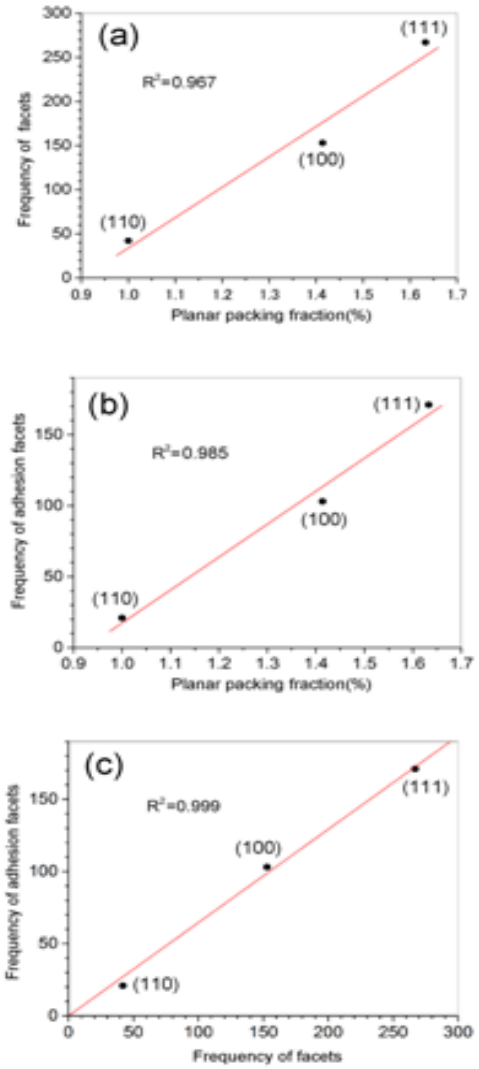

Fig. 13. (a) Observed frequency of Pt NP facets plotted as a function of Pt planar packing fraction (%). (b) Observed frequency of Pt NP-CB adhesion facets plotted as a function of Pt planar packing fraction (%). (c) Observed frequency of Pt-CB adhesion facets plotted as a function of the observed frequency of Pt NP facets.

Next, to elucidate the influence of CB surface tension on the strain of Pt NPs, the (111) interplanar spacing was measured as a function of orientation relative to the Pt NP-CB adhesion interface for the 97 Pt NPs observed in the FIB-processed TEC10E50E powder.

The orientation of the (111) plane was defined as shown in Fig. 14 (a), using the azimuth angle, θ (°). Figure 14 (b) shows the strain distribution of 175 (111) planes of Pt NPs measured as a function of azimuth, θ, where the (111)

interplanar strain (%) was defined as $100(d_{111}-0.2265)/0.2265$ for a measured spacing d_{111} (nm) of a (111) lattice plane. The mean strain was calculated to be -1.6 %. We note that no correlation can be observed between the (111) interplanar strain and the azimuth angle, indicating that the (111) interplanar strain does not depend on the orientation of the (111) planes and that the surface tension of CB particles does not exert a marked influence on the strain of the Pt NPs. It is suggested that the Pt NPs are spontaneously strained and that the surface tension caused by CB particles is negligible and too small to induce anisotropic strain in Pt NPs.

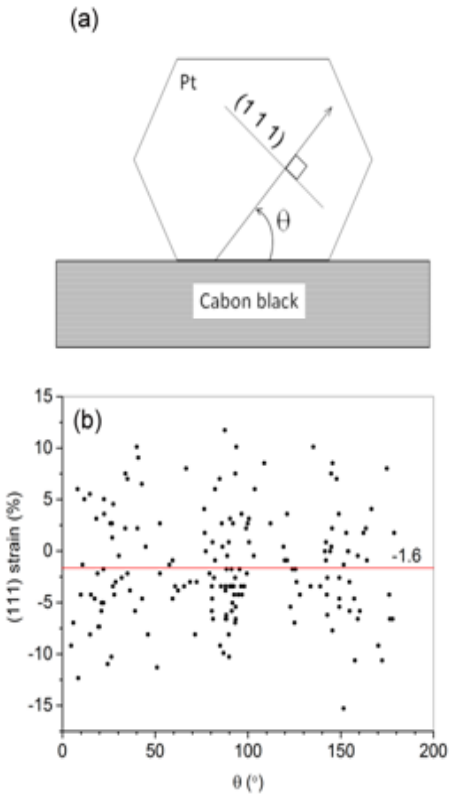

Fig. 14 (a) Azimuth angle, θ (°), normal to the (111) plane of a Pt NP measured from the Pt NP-CB adhesion interface. (b) (111) interplanar strain (%) of Pt NPs from the FIB-processed TEC10E50E powder plotted as a function of azimuth, θ.

Reported surface energy values of CB range from 20.55 mJ/m^2 to 96.20 mJ/m^2 [16], while the mean surface energy of the (111), (100) and (110) facets of Pt is 2.49 ± 0.26 J/m^2 [15]. Hence, we consider that the surface tension of CB particles was not strong enough to cause marked strain in the Pt NPs. However, instead of using the Pt NPs chemically loaded onto CB particles, it is also possible to use clean surfaces of carbon substrates to which Pt NPs can directly adhere in order to better understand the influence of the surface tension of carbon substrates on the structure of Pt NPs. For this purpose, the deposition of Pt NPs on carbon substrates using a coaxial arc plasma gun in vacuum is a suitable method of investigating the interaction between the Pt NP surface and carbon substrate surface. These experiments are currently in process.

IV. CONCLUSION

(1) The crystal structure of Pt NPs on TEC10E50E was observed by HRTEM. The structures of the Pt NPs were found to be inhomogeneously strained. The lattice parameters of Pt NPs were calculated, assuming monoclinic structures. No correlation was observed between the monoclinic lattice parameters and the diameter of the Pt NPs. About 80 % of the Pt NPs were compressively strained, and about 20 % of the Pt NPs were expansively strained.

(2) To investigate how the Pt NPs are adhered to the CB particles, side-view HRTEM images of Pt NPs were analyzed. The (111), (100) and (110) facets of the Pt NPs were observed to be adhered to CB particles. The frequency of adhesion interfaces decreased in the order of (111), (100), and (110) facets. This order was consistent with the (111), (100), and (110) planar packing fractions of Pt, the observed frequencies of (111), (100), and (110) facets of Pt NPs, and the (111), (100), and (110) surface energies of Pt.

(3) The variation of (111) interplanar spacing of Pt NPs on CB particles was analyzed as a function of azimuth angle from the Pt NP-CB adhesion interface. No correlation was observed between the variation of (111) interplanar spacing and the azimuth, which implies that the Pt NPs are spontaneously strained without being influenced by the CB particles whose surface tension is not strong enough to deform the Pt NPs.

ACKNOWLEDGEMENTS

A part of this work was conducted at Advanced Characterization Nanotechnology Platform of the University of Tokyo and National Institute for Materials Science (Japan), supported by Nanotechnology Platform of the Ministry of Education, Culture, Sports, Science and Technology (MEXT), Japan. This study is based on the results obtained from a project commissioned by the New Energy and Industrial Technology Development Organization (NEDO). The authors are grateful to Mr. Makoto Mori (TUS), Mr. Yuta Nakajo (TUS) and Mr. Yorito Nishizawa (TUS) for preparing samples for TEM observations.

REFERENCES

[1]. I. N. Leontyev, A. B. Kuriganova, N. G. Leontyev, L. Hennet, A. Rakhmatullin, N. V. Smirnova, V. Dmitriev, Size dependence of the lattice parameters of carbon supported platinum nanoparticles: X-ray diffraction

analysis and theo-retical considerations, RSC Adv., 4, 2014, 35959-35965.

[2]. K. Miyazawa K, M. Yoshitake, Y. Tanaka, HRTEM analyses of the platinum nanoparticles prepared on graphite particles using coaxial arc plasma deposition, J. Nanopart. Res., 19, 2017, 191.

[3]. K. Miyazawa, M. Yoshitake, Y. Tanaka, Characterisation of platinum nanoparticles deposited on C_{60} fullerene nanowhiskers. Surf. Eng., 34, 2018, 846-851.

[4]. T. Daio, A. Staykov, L. Guo, J. Liu, M. Tanaka, S. M. Lyth, K. Sasaki K, Lattice strain mapping of platinum nanoparticles on carbon and SnO_2 supports, Sci. Rep., 5, 2015, 13126.

[5]. M. Mavrikakis, B. Hammer, J. K. Nørskov, Effect of strain on the reactivity of metal surfaces, Phys. Rev. Lett., 81, 1998, 2819.

[6]. L. Bu, N. Zhang, S. Guo, X. Zhang, J. Li, J. Yao, T. Wu, G. Lu, J.-Y. Ma, D. Su, X. Huang, Biaxially strained PtPb/Pt core/shell nanoplate boosts oxygen reduction catalysis, Science, 354, 2016, 1410-1414.

[7]. V. Tripković, I. Cerri, T. Bligaard, J. Rossmeisl, The influence of particle shape and size on the activity of platinum nanoparticles for oxygen reduction reaction: A density functional theory study, Catal. Lett., 144, 2014, 380–388.

[8]. N. M. Markovic, R. R. Adžić, B. D. Cahan, E. B. Yeager, Structural effects in electrocatalysis: oxygen reduction on platinum low index single-crystal surfaces in perchloric acid solutions, J. Electroanal. Chem, 377, 1994, 249-259.

[9]. K. Miyazawa, H. Satsuki, M. Kuwabara, M. Akaishi, Microstructural analysis of high-pressure compressed C_{60}, J. Mater. Res. 16, 2001, 1960-1966.

[10]. V. A. Sethuraman, J. W. Weidner, A. T. Haug, M. Pemberton, L. V. Protsailo, Importance of catalyst stability vis-à-vis hydrogen peroxide formation rates in PEM fuel cell electrodes, Electrochim. Acta, 54, 2009, 5571-5582.

[11]. F. Liu, C. Wu, G. Yang, S. Yang, CO oxidation over strained Pt(100) surface: A DFT study, J. Phys. Chem. C, 119, 2015, 15500−15505.

[12]. X. Wang, Y. Orikasa,Y. Takesue, H. Inoue, M. Nakamura, T. Minato, H. Hoshi, Y. Uchimoto, Quantitating the lattice strain dependence of monolayer Pt shell activity toward oxygen reduction, J. Am. Chem. Soc., 135, 2013, 5938–5941.

[13]. S. Kattel, G. Wang, Beneficial compressive strain for oxygen reduction reaction on Pt (111) surface, J. Chem. Phys., 141, 2014, 124713-1-124713-8.

[14]. Ch. V. Rao, B. Viswanathan, Monodispersed platinum nanoparticle supported carbon electrodes for hydrogen oxidation and oxygen reduction in proton exchange membrane fuel cells, J. Phys. Chem. C, 114, 2010, 8661-8667

[15]. A. Patra, J. E. Bates, J. Sun, J. P. Perdew, Properties of real metallic surfaces: Effects of density functional semilocality and van der Waals nonlocality, PNAS 114, 2017, E9188-E9196.

[16]. M. Mezgebe, Q. Shen, J.-Y. Zhang, Y.-W. Zhao, Liquid adsorption behavior and surface properties of carbon blacks, Colloid. Surface. A, 403, 2012, 25-28.

Kun'ichi Miyazawa,"Structure and Facet Characterization of Platinum Nanoparticles Loaded on Carbon Black Particles using HRTEM "International Journal of Engineering Research and Applications (IJERA) , vol. 8, no.11, 2018, pp 13-21